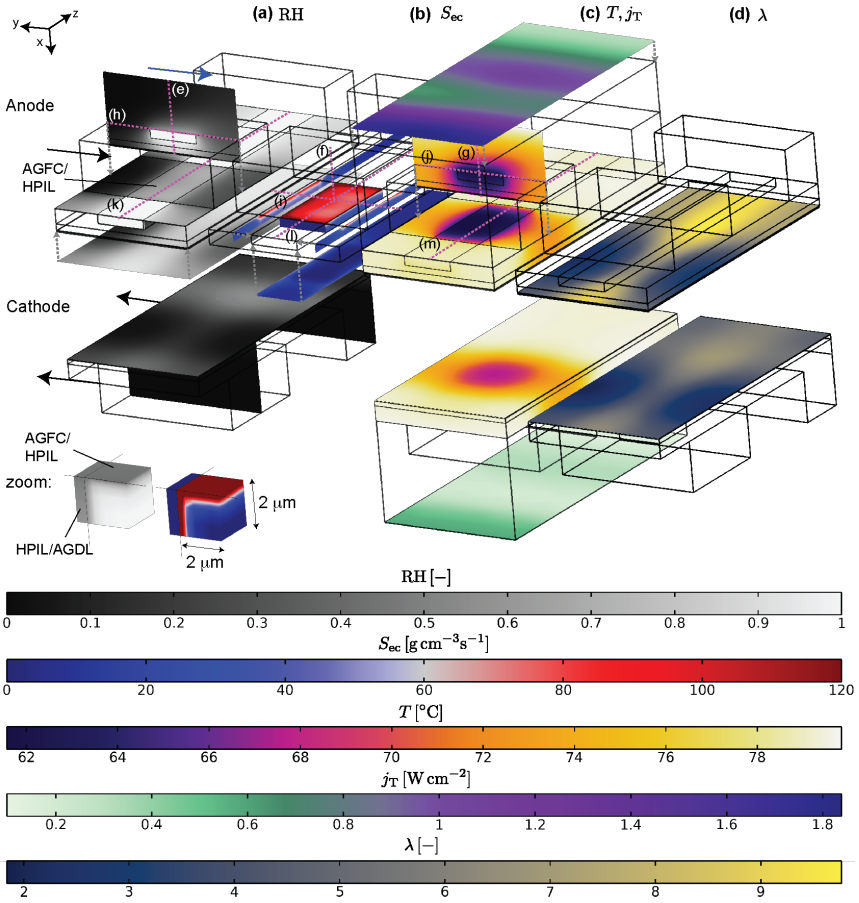
Schweizerische Eidgenossenschaft
Confédération suisse
Confederazione Svizzera
Confederaziun svizra

Federal Department of the Environment, Transport Energy and Communication DETEC

Swiss Federal Office of Energy SFOE
Energy Research and Cleantech Division

Final report dated 22 September 2022

Development and **Ma**rketing of **P**roton **E**xchange **M**embrane Fuel Cell Models for Transport Applications (DeMaPEM)



A main goal of the DeMaPEM project was to develop a 3-D single cell model of a proton exchange membrane fuel cell. We have set up a 3-D model to improve our understanding of the transport of water and heat in an evaporative cooling cell. This figure shows the simulated distribution of (a) relative humidity, (b) evaporation rate, (c) temperature and heat flux, and (d) dissolved water in the ionomer.

Jürgen O. Schumacher and Robert Herrendörfer, Institute of Computational Physics, ZHAW 2022



Date: 22 September 2022

Location: Bern

Publisher:
Swiss Federal Office of Energy SFOE
Energy Research and Cleantech
CH-3003 Bern
www.bfe.admin.ch

Subsidy recipients:
Zurich University of Applied Sciences ZHAW
Institute of Computational Physics ICP
Wildbachstrasse 21, CH-8401 Winterthur
https://www.zhaw.ch/icp

Authors:
Jürgen O. Schumacher, ZHAW-ICP, schm@zhaw.ch
Robert Herrendörfer, ZHAW-ICP, herf@zhaw.ch

SFOE project coordinators:
Rolf Schmitz, rolf.schmitz@bfe.admin.ch
Stefan Oberholzer, stefan.oberholzer@bfe.admin.ch

SFOE contract number: SI/501764-01

The authors bear the entire responsibility for the content of this report and for the conclusions drawn therefrom.



Summary

The project DeMaPEM aimed at the development and marketing of numerical models of proton exchange membrane fuel cells (PEMFCs) for transport solutions. We have created 2-D and 3-D single cell models to simulate the evaporative water removal from the PEMFC. In a first study, we simulated ex-situ experiments of evaporation in gas diffusion layers of PEMFCs. In a second study, we analyzed the water and heat transport in evaporative cooling cells. Cooperation with the PSI in both studies allowed us to compare our simulation results to experimental data and to improve our modeling method. Results showed the impact of operating conditions and carrier gas species on the evaporation rate and provided insights into the transport of water vapor. Furthermore, we demonstrated the importance to account for the heat transport to avoid overestimating evaporation rates.

In this final report, we also document our progress in the preparation of the Swiss spin-off company named Isomorph. Therefore, we have developed a new website and web services of isomorph.ch to market computational solutions for two different electrochemical flow cell types, that is PEMFCs and redox flow batteries. For these flow cell types, we worked out costumer-oriented product and service descriptions. Furthermore, we wrote a first version of a business plan.

Some models with generic parameterisations were made available to the research community as open-source code via a GitHub software repository related to Isomorph.

Main findings

- New 2-D and 3-D numerical models were developed and applied to study evaporative water removal in PEMFCs providing insights into the water and heat transport.
- A new website of isomorph.ch and web services were created to market computational solutions for PEMFCs and redox flow batteries.
- Costumer-oriented product and service descriptions were worked out and a business plan was written, preparing the founding of the Swiss spin-off company Isomorph.
- A GitHub software repository was created to make open-source codes available to the research community.

Contents

Summary 3

Main findings 3

Abbreviations 5

1 Introduction 6

1.1 Background information and current situation . . . 6

1.2 Purpose of the project . . . 6

1.3 Objectives . . . 6

2 Procedures and methodology 8

2.1 Modeling mass and heat transport due to water evaporation . . . 8

2.2 Dynamic GDL/GFC liquid water egress boundary condition . . . 11

3 Results and discussion 15

3.1 Transport of water and heat due to evaporation . . . 15

3.2 Droplet formation and growth . . . 25

3.3 GitHub software repository . . . 25

3.4 Preparation of spin-off company . . . 25

4 Conclusions 28

5 Outlook and next steps 28

5.1 Multi-scale two-phase simulations . . . 28

5.2 3-D single cell model with electrochemical reactions . . . 28

5.3 Improved model parameterisation and MEA degradation modeling . . . 28

5.4 Isomorph.ch . . . 29

5.5 Business plan . . . 29

6 National and international cooperation 29

7 Publications 29

References 30



Abbreviations

1D-MMM	1-D master MEA model
1D-PMM	1-D parametrized MEA model
2D-ATC-S	2-D along the channel model
2D-EvaGDL	2-D model to study evaporation in GDLs
3D-EvaCool	3-D evaporative cooling model
3D-EvaGDL	3-D model to study evaporation in GDLs
ACL	Anode catalyst layer
AGDL	Anode gas diffusion layer
AMPL	Anode micro porous layer
CCL	Cathode catalyst layer
CGDL	Cathode gas diffusion layer
CMPL	Cathode micro porous layer
CL	Catalyst layer
ED	Evaporation domain
FCP	Flow channel plate
GDL	Gas diffusion layer
GFC	Gas flow channel
HPIL	Hydrophilic line
ICP	Institute of Computational Physics
MEA	Membrane electrode assembly
PEM	Proton exchange membrane
PEMFC	Proton exchange membrane fuel cell
PSI	Paul Scherrer Institut
ZHAW	Zurich University of Applied Sciences



1 Introduction

1.1 Background information and current situation

Companies are working worldwide on fuel cell powered transport solutions with hydrogen technology and electric drive (Figure 1). These include passenger vehicles, buses, trucks, hydrogen fueled trains, ships and aircrafts. The membrane electrode assembly (MEA) is a crucial part of proton exchange membrane fuel cells (PEMFCs). To develop competitive products, MEA manufacturers need to determine the process and material-specific energy conversion losses. However, most manufacturers currently only obtain empirical relationships from analyzing experimental performance data of MEAs and single test cells. These empirical relationships provide limited insight into physico-chemical limitations of power density.

1.2 Purpose of the project

The purpose of the project was to develop and market computational solutions of MEAs and single test cells to analyze the MEA components based on their physical and electrochemical properties and the governing processes. Prior to this project, a 1-D steady-state master MEA model (1D-MMM) was developed in our group, which was published as a free and open source code [1]. Subsequently, Vetter and Schumacher extended this model to a parameterized MEA model (1D-PMM) by including diverse material parameterization from literature [2]. Its use was demonstrated in a fast computation of a local and global sensitivity analysis that allowed to identify the membrane properties as critical parameters for assessing the performance of PEMFCs [3].

1.3 Objectives

The goal of this project was to improve the 1D-PMM, focusing on two aspects (Figure 1). We wanted to improve the description of the egress of liquid water from the porous gas diffusion layer (GDL) to the gas flow channel (GFC). This is essential to predict the flow of liquid water produced during fuel cell operation, which is especially important at high current densities. Furthermore, the goal was to develop a 3-D single cell model. This is a necessary step to study the role of geometrical modifications of the MEA, the channel-rib structure, and the importance of anisotropic model parameters. This 3-D model was applied to analyze the transport of water and heat induced by evaporation in gas diffusion layers (GDLs). On the marketing side, the goal was to prepare a new Swiss spin-off company of ZHAW with the name Isomorph by improving the website isomorph.ch to announce products and services and by writing a business plan that includes the marketing strategy and market analysis. Furthermore, we aimed to transfer our scientific knowledge by creating a GitHub software repository.

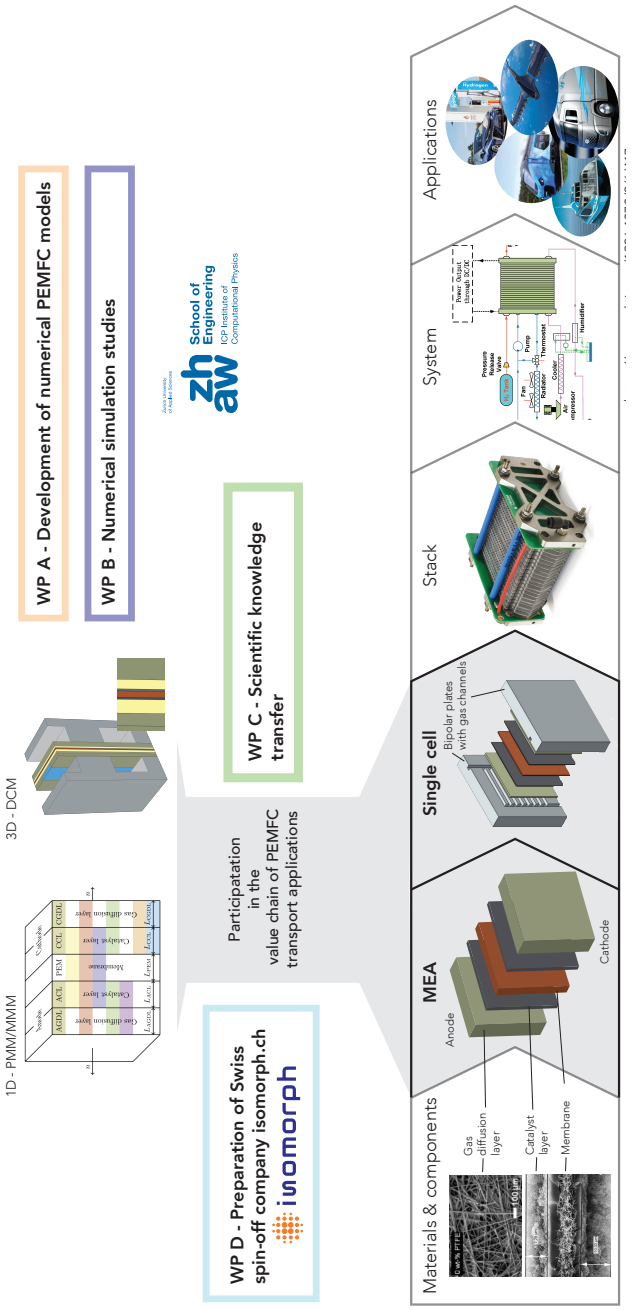


Figure 1: Project overview, including the four work packages (WP), and the international value chain of PEMFCs for transport applications. The goal is the development of two computational models of PEMFCs with a focus on MEAs and single cells. The marketing of these computational solutions by the Swiss spin-off company Isomorph and the scientific knowledge transfer will allow us to participate in the international value chain.



2 Procedures and methodology

In this project, numerical models were developed to simulate the transport of water and heat induced by evaporation (section 2.1) and to better understand the dynamics of liquid water at the GDL/GFC interface (section 2.2).

2.1 Modeling mass and heat transport due to water evaporation

The goal of this project was to develop a 3-D model of a single cell. As part of this development, we focused on the simulation of mass and heat transport due to water evaporation. Water evaporation is an important process in polymer electrolyte fuel cells to (i) remove product water from electrochemical reactions in gaseous form from the CLs and (ii) in modified GDLs in evaporative cooling cells to allow for simultaneous cooling and humidification [4].

2.1.1 Evaporative cooling cell model: 3D-EvaCool

A promising concept to optimize water and heat management of PEMFCS is evaporative cooling [5–7]. It is based on the evaporation of water directly inside the cell and the simultaneous dissipation of latent heat. One of the evaporation cooling concepts was developed at the Paul Scherrer Institute, which is solely based on the modification of the wettability in a gas diffusion layer (GDL) [8–11]. The wetting properties are locally turned from hydrophobic to hydrophilic within separated parallel lines, which are placed perpendicular to the gas flow channels (GFCs) (Figure 2a). These hydrophilic lines (HPILs) can wick water from a liquid water channel (LWC) within the anode flow field. The water in the HPILs then evaporates and, hence, provides simultaneous humidification and cooling. This concept has been investigated in experiments. Cochet et al. [4] focused on the evaporation in a complete but non-operating thermal test cell (i.e. without electric current). They measured the heat flux on the anode and cathode side at different anode and cathode gas speeds. The total heat flux for gas speeds representative of a long cell behavior was higher than 1 Wcm^{-2} and, hence, in the same order of magnitude as the waste heat released by an operating PEMFC. While these experiments and the analytical model provided a lot of insights into the evaporation cooling concept, only the heat flux was measured at the ends of the anode and cathode flow channel plate (FCP). No measurements were done or are possible for the distribution of temperature and relative humidity inside the cell, evaporation along the HPILs, water vapor transport paths and membrane humidification.

Therefore, we have developed a 3-D macro-homogeneous numerical model of an evaporative cooling cell (referred to as 3D-EvaCoolCell). This model contains all layers of the experimental evaporative cooling test cell of Cochet et al. [4], but focuses on one interface between a HPIL and GFC (Figure 2). In this non-isothermal two-phase model we solve for the conservation of mass and momentum of gas and liquid water, for the transport of gas species, for the conservation of energy, and for the transport of dissolved water in the ionomer of the catalyst layers and membrane using a parameterization extended from the work of Vetter and Schumacher [3]. Implementation has been done in COMSOL Multiphysics version 5.6 using finite elements with linear shape functions as discretization of the equations. The detailed method is described in Herrendörfer et al. [12].

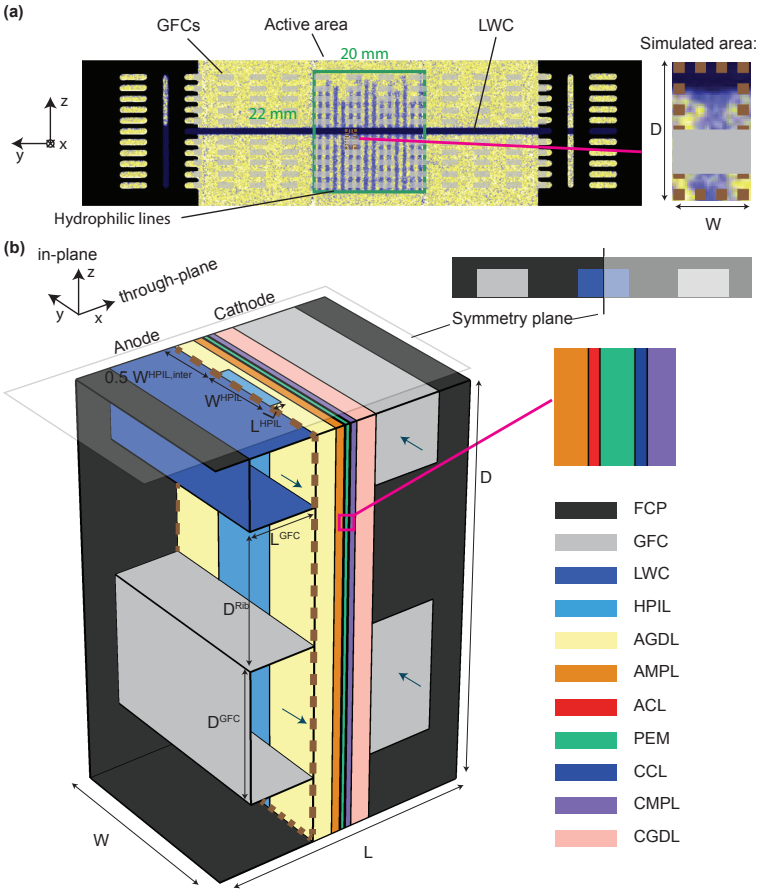


Figure 2: Experimental and numerical model setup of the evaporative cooling cell. (**a**) Neutron radiography image of the experimental setup of [4] with the view on the top of the anode gas diffusion layer (AGDL). (**b**) Numerical model setup. Dashed brown frame corresponds to the brown rectangle in (a).

2.1.2 Simulation of ex-situ experiments of water evaporation in a GDL

We have cooperated with the PSI to better understand evaporative water removal from PEMFCs. At PSI, direct evaporation rate measurements were performed from a differential ex-situ cell imitating a GDL and gas channel in a fuel cell. Figure 3 a shows the setup of the ex-situ experiments in Mularczyk et al. [13]. It consists of a flow flow field with a single GFC. Using a syringe pump and an injector, water is supplied to the base of a GDL. The evaporation domain (ED) is defined using a pool gasket with a rectangular cutout. A dry carrier gas (either H_2 or N_2) enters into the GFC. Liquid water from the pool was prevented to enter the GDL domain, resulting in pure gaseous transport through the GDL. The role of gas speeds, temperature and the evaporative domain on the evaporation rate were investigated.

Our part at ZHAW was to develop a numerical model to interpret the experimental results. In a first step, we assisted in the development of a 2-D, isothermal, macro-homogeneous along-the-channel model that takes into account Fickian diffusion in the GDL and gas channel under the assumption of

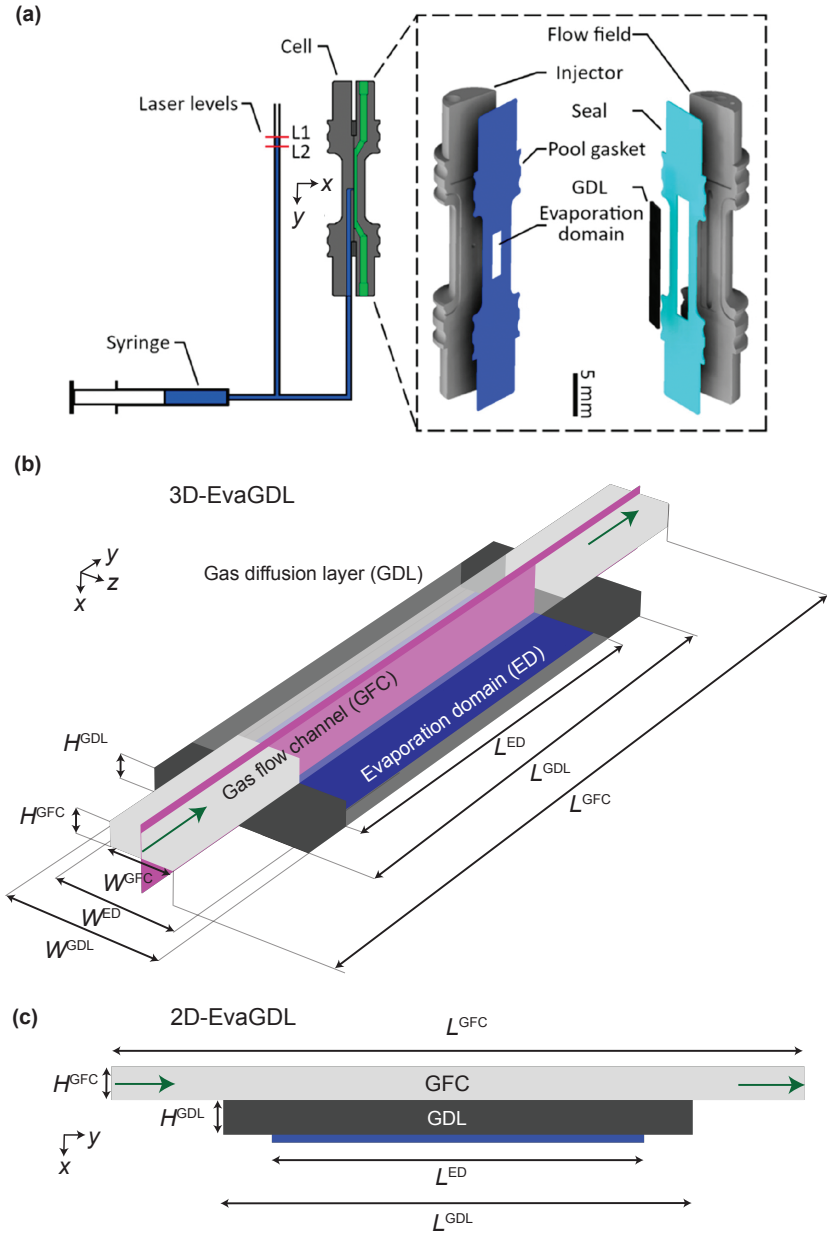


Figure 3: Experimental and model setups to study the evaporative water removal **(a)** Experimental model setup of Mularczyk et al. [13]. **(b)** Setup of the 3-D model, referred to as 3D-EvaGDL, to simulate the experiments of of Mularczyk et al. [13]. An evaporative domain is placed at the bottom of a gas diffusion layer (GDL). A dry carrier gas enters into the gas flow channel (GFC). The magenta plane is the symmetry plane of the setup exploited in the simulations to reduce computational costs. **(c)** Setup of the 2-D model, referred to as 2D-EvaGDL, that simulates evaporative water removal along the direction of the GFC. Green arrows indicate the flow direction in the GFC.



constant gas density and fully saturated interfacial area, and predefined convection in the gas channel. This simple but fast model, that is described in detail in reference [13], is referred to as 2D-ATC-S.

As a next step, this model was extended to account for the full set of conservation equations including the conservation of mass, momentum and energy. This model, which is described in reference [14] (manuscript attached to this report), is referred to as 2D-EvaGDL. In the 3-D model called 3D-EvaGDL we analyzed the contribution of the evaporation domain below the rib. Both models were implemented in COMSOL Multiphysics Version 5.6.

2.2 Dynamic GDL/GFC liquid water egress boundary condition

One goal of this project was to derive liquid water egress boundary conditions for liquid water at the GDL/GFC interface suitable for the use in macro-homogeneous PEMFC models.

We have conducted a literature study on the published models on the treatment of the liquid water at the interface between GDL and GFC. Esposito et al. [15] presented a lumped model for the transport of liquid water through a PEMFC, which includes the liquid water transport at the interface between GDL and GFC. At this interface, simulated droplets can form, coalesce and finally detach from the interface. To better understand this model proposed by Esposito et al. [15], we have implemented it in Matlab. The evaluation of this Matlab implementation lead to following points of criticisms of the model:

- The model of [15] does not resolve the individual layers in space.
- There is no coupling between the GFC/GDL interface and the electrochemical reaction in the CL.
- The droplet growth does not follow the Young-Laplace law.

Therefore, we have developed a new model based on previous work in our group [16]. In Figure 4, the concept of our model is shown. By assuming a constant gas pressure and relative humidity within the gas flow channel (GFC), the problem can be represented by a 1-D model consisting only of catalyst layer (CL) and a gas diffusion layer (GDL). This 1-D model is coupled with a 2-D GDL/GFC interface model to simulate the formation and growth of water droplets due to the liquid water generated from the electrochemical reaction in the CL.

Governing equations: These two layers represent in a simple form the cathode of a PEMFC. In these two layers, we solve for the isothermal (T=70 ℃) two-phase flow of gas and liquid water using the so called two-fluid model, which consists of two independent Darcy equations for the liquid and gas phase:

$$\frac{\partial}{\partial t}\left(\varepsilon_p s_\beta \rho_\beta\right) + \nabla \cdot \left(\rho_\beta u_\beta\right) = S_\beta \tag{1}$$

$$u_\beta = -\frac{\kappa_{\mathrm{abs}} \kappa_{\mathrm{rel},\beta}}{\mu_\beta} \nabla P_\beta \tag{2}$$

where ε_p and κ_{abs} are the porosity and absolute permeability, and $u_\beta, P_\beta, S_\beta, s_\beta, \rho_\beta$ and $\kappa_{\mathrm{rel},\beta}$ are the velocity, pressure, source term, saturation, density and relative permeability of the gas (β=gas) and liquid phase (β=liq), respectively. The relative permeabilities are defined as

$$\kappa_{\mathrm{rel,liq}} = s_{\mathrm{liq}}, \quad \kappa_{\mathrm{rel,gas}} = s_{\mathrm{gas}} = 1 - s_{\mathrm{liq}}. \tag{3}$$

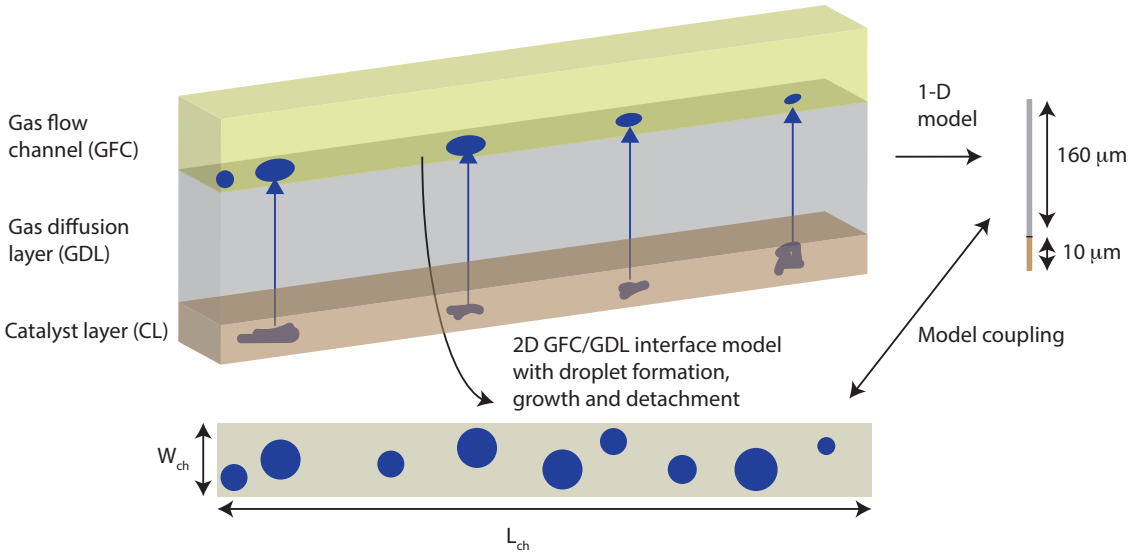


Figure 4: Model concept to investigate the liquid water boundary condition at the interface between GDL and GFC.

The capillary pressure is defined as

$$P_\mathrm{c} = P_\mathrm{liq} - P_\mathrm{gas}. \tag{4}$$

P_c determines the liquid water saturation in the CCL and GDL, which is shown in Figure 5. The mass

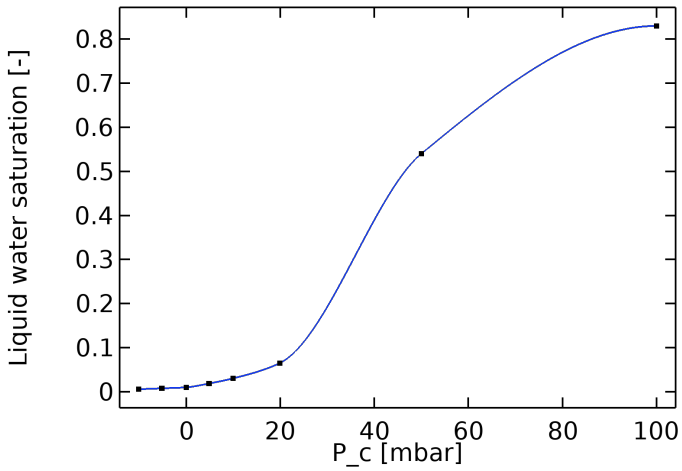


Figure 5: Liquid water saturation s_liq as a function of capillary pressure P_c.

conservation of the gas species X (N_2, H_2O and O_2) is expressed for mass concentrations ω_X as

$$\frac{\partial}{\partial t}\left(\rho_\mathrm{gas}\omega_X\right) + \nabla \cdot j_X + \nabla \cdot \left(\rho_\mathrm{gas}\omega_X u_\mathrm{gas}\right) = S_X \tag{5}$$

We solve for the mass fraction of H_2O and O_2, so that

$$\omega_{\mathrm{N}_2} = 1 - \omega_{\mathrm{O}_2} - \omega_{\mathrm{H_2O}} \tag{6}$$



The diffusive flux is described using Fick's law as:

$$j_X = -\rho_{\text{gas}} D_X \nabla \omega_X \tag{7}$$

where D_X is the Fickian diffusivity defined as:

$$D_X = M_p D_{X,\text{ref}} \frac{T}{T_{\text{ref}}} \frac{P_{\text{ref}}}{P_{\text{gas}}} \tag{8}$$

with $T_{\text{ref}} = 80\,$℃. The microstructure factor is defined as [1]

$$M_p = \frac{\varepsilon_{\text{p}}}{\tau_{\text{p}}^2}(1 - s_\beta)^3 \tag{9}$$

and

- $D_{\text{O}_2,\text{ref}} = 0.28$ cm^2/s for oxygen in air
- $D_{\text{H}_2\text{O},\text{ref}} = 0.36$ cm^2/s for water vapor in air
- $D_{\text{N}_2,\text{ref}} = 0.29$ cm^2/s for nitrogen in air

S_i is zero for all species except of O_2 such that $S_{\text{gas}} = S_{\text{O}_2}$. Instead of accounting for the electrochemical reaction in a PEMFC, we choose to define ad-hoc the source term for liquid water production S_{liq} in the catalst layer depending on the oxygen partial pressure p_{O_2} and liquid water saturation and couple this to the consumption of O_2 as:

$$S_{\text{liq}} = -S_{\text{gas}} = -S_{\text{O}_2} = 3000 \left[\frac{\text{mg}}{\text{cm}^3\text{s}}\right] (1 - s_{\text{liq}}) \frac{p_{\text{O}_2}}{P_{\text{ref}}} \tag{10}$$

where P_{ref} is the reference pressure of 1 atm. In the CGDL, the source term is zero. The gas density ρ_{gas} is defined assuming the ideal gas law as

$$\rho_{\text{gas}} = M_{\text{n}} \frac{P_{\text{gas}}}{RT}, \tag{11}$$

where the mean molar mass is

$$M_{\text{n}} = \frac{1}{\sum_X^N \frac{\omega_X}{M_X}}. \tag{12}$$

The domain parameters are listed in Table 1. Operating conditions are listed in Table 2.

Table 1: Properties of the model domains.

Symbol	Explanation	Unit	CCL	CGDL
ε_{p}	Porosity	-	0.75	0.75
τ_{p}	Tortuosity	-	1.6	1.6
κ_{abs}	Absolute permeability	m^2	10^{-13}	10^{-13}



Table 2: Operating conditions

Symbol	Explanation	Value	Unit
$P_{\mathrm{gas,B}}$	Gas pressure at GDL/GFC interface	1.0	atm
T	Temperature	70	℃
$\mathrm{RH_C}$	Relative humidity at GDL/GFC interface	1	-
$\alpha_{\mathrm{O_2}}$	Mole fraction of oxygen in dry gas	0.21	-

Boundary conditions: No flux boundary conditions are defined at the outer boundary of the CCL. At the GDL/GFC interface, we define the following boundary conditions

- $P_{\mathrm{gas}} = P_{\mathrm{gas,B}}$
- $\omega_{\mathrm{O_2}} = \alpha_{\mathrm{O_2}} \left(1 - \frac{RH_{\mathrm{C}} P_{\mathrm{sat}}(T)}{P_{\mathrm{gas,B}}}\right) \frac{M_{\mathrm{O_2}}}{M_{\mathrm{n}}}$
- $\omega_{\mathrm{H_2O}} = \frac{RH_{\mathrm{C}} P_{\mathrm{sat}}(T)}{P_{\mathrm{gas,B}}} \frac{M_{\mathrm{H_2O}}}{M_{\mathrm{n}}}$

Finally, we arrive at defining the boundary condition for liquid water at the interface between GDL and GFC. As in the rest of the model, the normal liquid water velocity needs to fulfill

$$u_{\mathrm{liq,B}} = -\frac{\kappa_{\mathrm{abs}} \kappa_{\mathrm{rel,liq}}}{\mu_{\mathrm{liq}}} \nabla_x P_{\mathrm{liq}} \tag{13}$$

Under the assumptions of

- $\nabla_x P_{\mathrm{gas}}$=0, such that $\nabla_x P_{\mathrm{liq}} = \nabla_x P_{\mathrm{c}}$,
- $\nabla_x P_{\mathrm{c}} = \frac{P_{\mathrm{c,B}} - P_{\mathrm{c}}}{D_{\mathrm{BC}}}$, where D_{BC} is a characteristic length scale at the boundary between the GFC and GDL,

we can simplify this equation to [16]

$$u_{\mathrm{liq,B}} = -\frac{\kappa_{\mathrm{abs}} \kappa_{\mathrm{rel,liq}}}{\mu_{\mathrm{liq}}} \frac{P_{\mathrm{c,B}} - P_{\mathrm{c}}}{D_{\mathrm{BC}}}. \tag{14}$$

The outflow of the liquid water at the boundary is integrated over time to the droplet volume

$$V_{\mathrm{out}} = A_{\mathrm{active}} \int u_{\mathrm{liq,B}} \, \mathrm{d}t \tag{15}$$

where $A_{\mathrm{GFC/GDL}} = 0.2\,\mathrm{cm}^2$ is the interface area between the GDL and the GFC, assuming a channel thickness of 1 mm and channel length of 20 mm. Here we consider that the water egress leads to the formation and growth of a single droplet. The growth of a single droplet is governed by the Young-Laplace law. Before the droplet is formed, the capillary pressure increases as function of the water volume. Figure 6 shows the capillary pressure $P_{\mathrm{c,B}}$ as a function of water volume at the boundary during formation and growth of a single droplet.

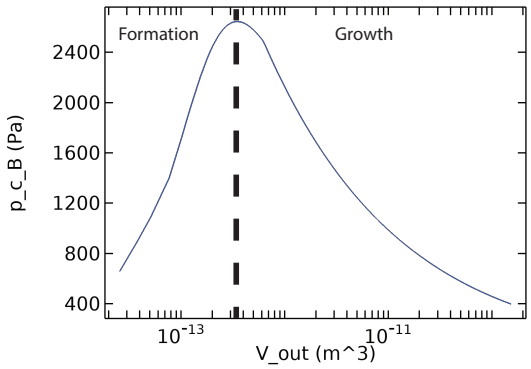


Figure 6: Capillary pressure at the GFC/GDL interface as a function of the outflow water volume.

Implementation We have implemented this 1-D model in COMSOL Multiphysics. The non-linear set of equations are solved using undamped Newton iterations and the PARDISO direct linear solver. The Newton iterations are stopped once the solution and residual error become lower than 10^{-7}. The model domain is meshed using 20 finite elements in both the CL and GDL, each with a symmetric distribution consisting of a geometric sequence of growing elements from the border to the center with an an element ratio of 10. First, a steady-state solution is obtained setting $V_{\text{out}} = 0$. This solution is then used as an initial condition for the time-dependent solver.

3 Results and discussion

3.1 Transport of water and heat due to evaporation

3.1.1 Simulation of an evaporative cooling cell using 3D-EvaCool

Using the developed model 3D-EvaCool, we analyzed the transport of water and heat in an evaporative cooling cell. In the following, we provide a shortened version of the description of the results in reference [12].

In the evaporative cooling cell, water is transported in liquid, vapor and dissolved phase, and is subject to evaporation and ab-/desorption phase changes. Liquid water from the LWC enters the MEA via the HPIL and is transported towards the AGFC where it evaporates. The evaporation rate varies locally (Figure 7b,f). It is the highest at the AGFC/HPIL interface. Furthermore, evaporation takes place along the HPIL/AGDL interfaces with the highest rates close to the AGFC. Close to the interfaces of the HPIL with the AGFC and AGDL, an evaporation film forms with a through-plane thickness of 0.7 μm (see zoom in Figure 7). Over this thickness, the evaporation rate decreases from its maximum at the respective interfaces to zero inside the HPIL (Figure 7f,i), while RH drops from being fully saturated inside the HPIL to unsaturated at the interfaces (Figure 7e,h).

The generated water vapor is transported not only in through-plane direction away from the AGFC/HPIL interface (Figure 8b,e) but also in y-direction (i.e. parallel to channel flow) away from the HPIL/AGDL interfaces (Figure 8c,i) and in z-direction (i.e. perpendicular to channel flow) towards the AGFC (Figure 8d,m). Correspondingly, RH decreases from the HPIL, where the gas is essentially

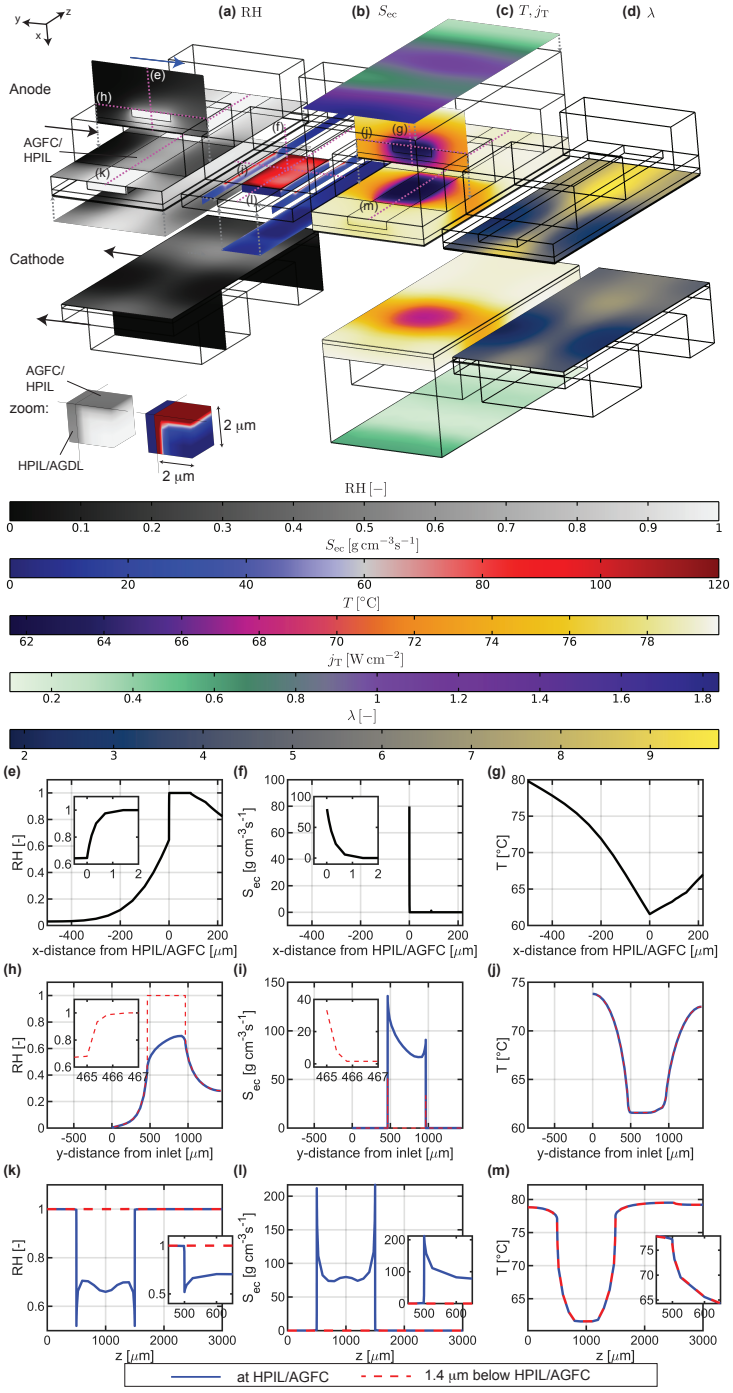


Figure 7: 3-D simulation results of the evaporative cooling cell using 3D-EvaCool: **(a)** relative humidity (RH), **(b)** evaporation rate (S_{ec}), **(c)** temperature (T) and conductive heat flux, and **(d)** the dissolved water content (λ). Anode and cathode are separated for visibility. Cubes of 2 μm length show a zoom of (a-b) at the triple junction of the gas flow channel (AGFC), hydrophilic line (HPIL) and gas diffusion layer (AGDL). **(e-m)** Profiles with orientation indicated with magenta dashed lines in (a-c): **(e-g)** through-plane profile; **(h-j)** y-profiles (parallel to channel) along and below the AGFC/HPIL interface; and **(k-m)** z-profile (perpendicular to channel).

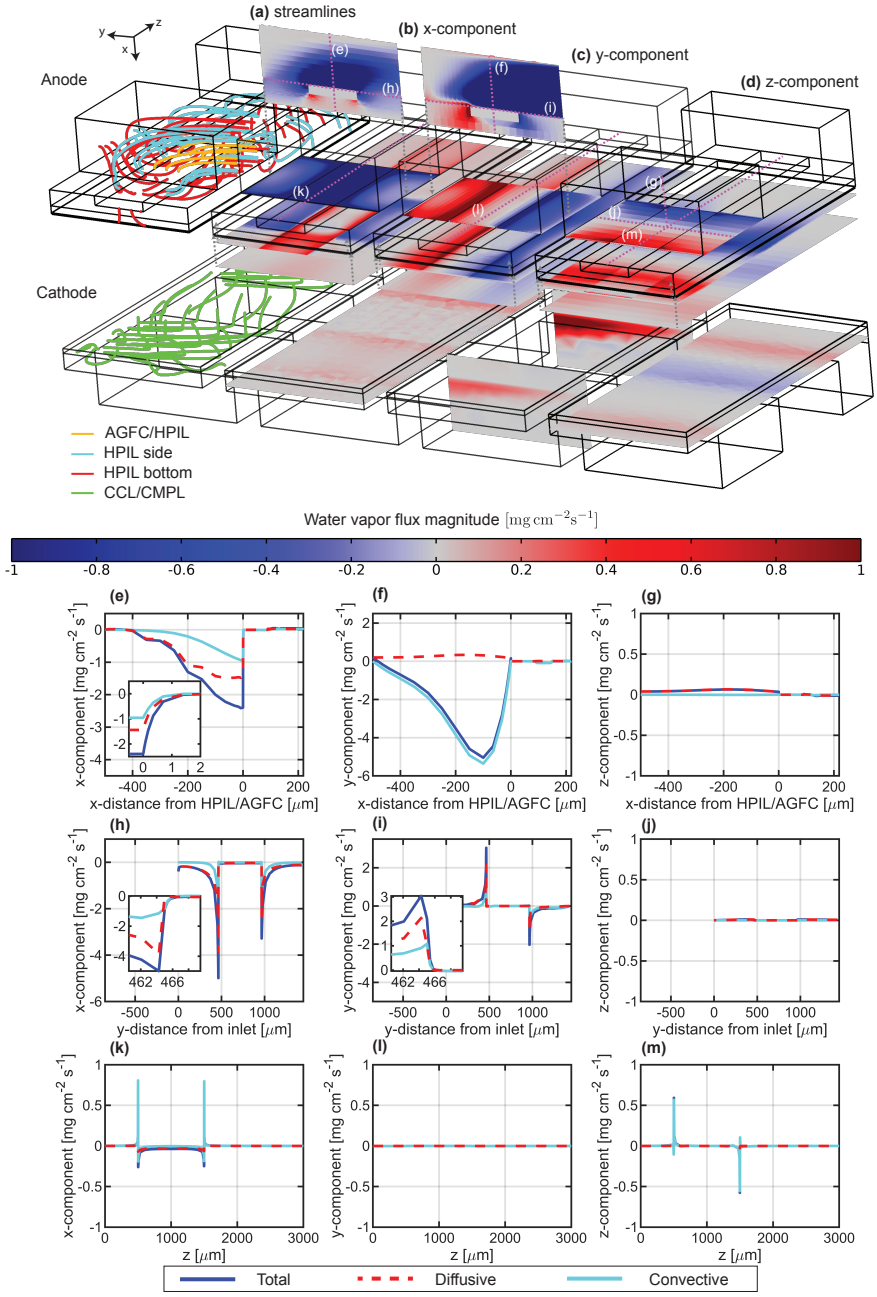


Figure 8: 3-D simulation results of the evaporative cooling cell using 3D-EvaCool: **(a)** streamlines of water vapor flux originating at different domain boundaries as indicated in the legend; total water vapor flux magnitude in **(b)** x-direction (through-plane), **(c)** y-direction (parallel to channel flow), and **(d)** z-direction (perpendicular to channel flow). **(e-m)** Profiles of water vapor flux components along profiles indicated with magenta dashed lines in (b-d).



fully saturated, towards the AGFC (Figure 7a). From the 75 mg h^{-1} leaving via the AGFC, 49 mg h^{-1} enter the AGFC via the interface with the HPIL (orange streamlines in Figure 8a). The other 26 mg h^{-1} enter the AGFC via the two interfaces with the hydrophobic AGDL and originate from the HPIL side walls (cyan streamlines in Figure 8a) and bottom wall (red streamlines in Figure 8a). The majority of the water vapor flux crossing the two AGFC/AGDL interfaces is close to the HPIL and channel walls (Figure 8b,h). Inside the AGFC, water vapor is advected with the gas stream towards the AGFC outlet (Figure 8c,f). The part of the water vapor generated at the bottom HPIL wall in larger distance to the AGFC is transported to the ACL where it is absorbed into the ionomer. The distribution of the dissolved water content λ in the CL follows mainly the distribution of RH (Figure 7 a,d). The highest values are located at the projected intersection of the HPIL with the ribs and LWC. The lowest values can be found in the region of the projected AGFC/AGDL interface. The diffusive flux of λ in the PEM is the strongest in through-plane direction with the in-plane components being one order of magnitude smaller. In the CCL, λ follows a similar distribution than in the ACL at a lower level (Figure 7 d). Water vapor is desorbed from the ionomer in the CCL and transported towards the CGFCs where it is advected with the gas stream to the outlets (Figure 8a-d, bottom).

The transport mechanisms are influenced by the generation of a large amount of water vapor, which has a significantly higher molar mass than the carrier gas hydrogen. Corresponding to the distribution of RH (Figure 7a), ρ_{gas} and P_{gas} are higher inside the MEA than in the AGFC. Consequently, a convective flow develops from the HPIL towards the AGFC. The profiles of the water flux vector components in Figure 8e-m show that the convective contribution to the total water vapor flux is mostly smaller but of the same order of magnitude than the diffusive transport. Due to the absorption of water vapor into the ionomer of the ACL, P_{gas} is locally decreased such that an additional convective flow is directed from the HPIL to the ACL. The desorption of water vapor leads to an increase in P_{gas} in the CCL. The variations in P_{gas}, however, are significantly less than on the anode side due to smaller amount of water vapor and smaller difference in molar mass between water vapor and nitrogen. Therefore, diffusion is the dominant transport mechanism for water vapor on the cathode side of the MEA towards the CGFCs.

The temperature decreases due to the consumption of latent heat of evaporation. It reaches a minimum temperature of around 62 °C (Figure 7c), which is located at the center of the AGFC/HPIL interface (Figure 7g). This temperature drop from the operating temperature of 80 °C leads to a reduction in the strongly temperature-dependent saturation pressure by a factor of 2.2 (Figure 7k). This leads in turn to a reduction in the local evaporation rate. Close to the channel side walls there is a sharp temperature drop due to the contact of the channel with the highly thermally conductive FCP (Figure 7m), resulting in a high local heat flux and maximum evaporation rates close to the channel walls (Figure 7l). A comparison to an isothermal simulation shows that the overall evaporation rate is reduced from 156 mg h^{-1} to 82 mg h^{-1}. This demonstrates the importance of accounting for the transport of heat in an evaporative cooling cell.

The heat flux across the FCP ends is the highest in the regions within the ribs (Figure 7c) because the thermal conductivity in the FCP is much higher than thermal conductivity of the gas species in the GFCs. This channel-rib effect and local strong temperature gradients close to the AGFC/HPIL interface could be important for evaluating thermal stresses and related degradation mechanism.

Furthermore, we evaluated the role of the evaporation mass transfer coefficient. At high mass transfer coefficients a mass transport limitation is reached for water vapor through the MEA. In contrast, such limitation is not reached for the transport path via the GFC for the investigated range in transfer coefficients. An increase in mass transfer coefficient also leads to thinner evaporation films such that a further increase is limited by computational costs linked to the necessarily finer numerical mesh. This increasingly finer mesh could be avoided by developing a thin-film approximation of the evaporation-induced water and heat transport with the help of ex-situ experiments. This thin-film



approximation would allow to simulate larger domains with more HPILs and gas channels and to compare directly to the experiments of Cochet et al. [4].

In conclusion, our modeling results show that

- the temperature drop due to evaporation is not negligible also in the experiments and hence should be included in the calculation of the saturation pressure, and, hence, of the evaporation rate;
- evaporation at the side and bottom interfaces of the HPIL with the hydrophobic AGDL contributes to the total evaporation rate and to the water vapor flux towards the GFC outlets;
- the mass transport resistance due to ab-/desorption into/from the ionomer adds to the total mass transport resistance of water vapor towards the CGFC outlets.

3.1.2 Simulation of ex-situ experiments using 2D-ATC-S

Results are described in detail in the published article [13]. In the following, we provide a summary of the main results.

The evaporation rates simulated in the 2D-ATC-S model showed a good agreement with the experimental observed evaporation rates at different gas speed, evaporative domain lengths and temperatures (Figure 9). At low gas speed, evaporation rates are limited by the convective transport in the GFC when the GFC is fully saturated with water vapor, as indicated by the dashed line in Figure 9a. At high gas speed, the evaporation rate reaches a plateau. The interpretation supported by the model is that the evaporation rate is limited by the diffusion driven transport of water vapor in the GDL. The influence of the operating temperature on the evaporation rate at high gas speed could be explained by the change in diffusivity and saturation pressure.

Another important outcome of the model and the experiments is the relative contribution of the diffusion in the volume outside of the evaporative domain, which is the strongest for the shortest domains. Furthermore, the model was used to extrapolate to larger evaporation domains and higher temperatures than in the experiments. The model results demonstrated that the relative humidity increases over the evaporation domain in channel direction, leading to decreasing evaporation rates. Altogether, the experimental and modeling results highlight the importance of carefully analyzing the impact of the operating conditions when experimentally determining evaporation rates.

3.1.3 Simulation of ex-situ experiments using 2D-EvaGDL and 3D-EvaGDL

As the model 2D-ATC-S does not account for the full set of conservation equations and is limited to 2-D, we developed the models 2D-EvaGDL and 3D-EvaGDL to provide additional insights into the evaporative water removal. The goal was to conduct a more systematic analysis than in the previous studies. In the following, we provide a shortened version of the description of the results in reference [14] (attached manuscript).

In Figure 10a, the evaporation rate evaluated in the 2-D model, E_{2D}, is plotted as a function of the inlet gas speed for nitrogen and hydrogen as as carrier gas species, different operating temperatures, and evaporation domain sizes. Evaporation rates vary over more than two orders of magnitude over the investigated parameter range. The increase in evaporation rate with respect to the gas speed is

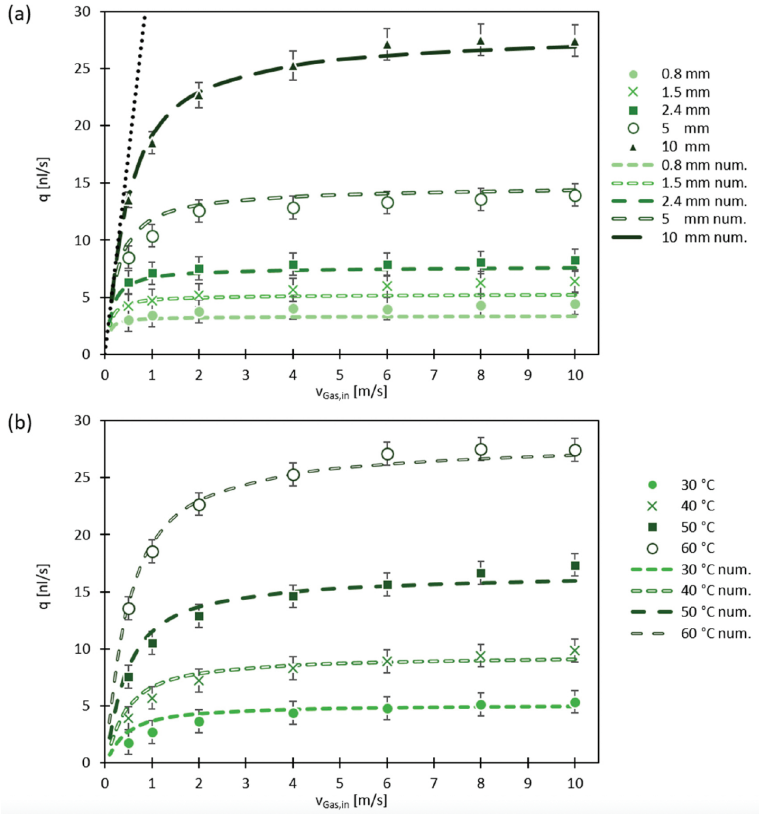


Figure 9: Evaporation rates q measured as a function of gas inlet velocities; **(a)** at a constant temperature of 60 °C for the measured evaporation domain lengths (markers) and the values obtained using the model 2D-ATC-S (dashed lines); **(b)** at a constant evaporation domain length of 10 mm at different operating temperatures. The dotted line in **(a)** indicates the maximum moisture carrying capability of the gas flow in the channel when fully saturated at 60 °C.

steep at the lowest gas speeds and levels off at increasing gas speeds. For the smallest evaporation domain, it becomes steeper again at the highest gas speeds. Generally, the evaporation rate increases for higher temperatures and larger evaporating domain sizes. Furthermore, it is higher under hydrogen than under nitrogen as expected from the higher diffusivity.

Figure 10c depicts the change in average relative humidity at the GFC outlet over the investigated parameter range. It approaches 1 at the lowest gas speeds and 0 at the highest gas speeds. Due to the higher evaporation rate, it is higher for increasing temperatures, larger evaporating domain sizes and under hydrogen than under nitrogen.

To obtain a more systematic understanding of the influence of the different parameters on the evaporation rate, we assume that evaporation is fully controlled by gas diffusion inside the GDL and convection in the GFC. On this basis derive expressions for two limits in evaporation rate. The first limit is related to the theoretical maximum through-plane diffusive water vapor flux. This limit is achieved when RH$\rightarrow 0$ at the GDL/GFC interface for $\lim_{U\rightarrow\infty}$. Considering that RH$\rightarrow 1$ at the interface between GDL and evaporation domain for $\sigma_{\mathrm{e}} \rightarrow 1$ and assuming that P_{gas} is constant throughout the GDL, we obtain for the maximum through-plane diffusive flux defined as

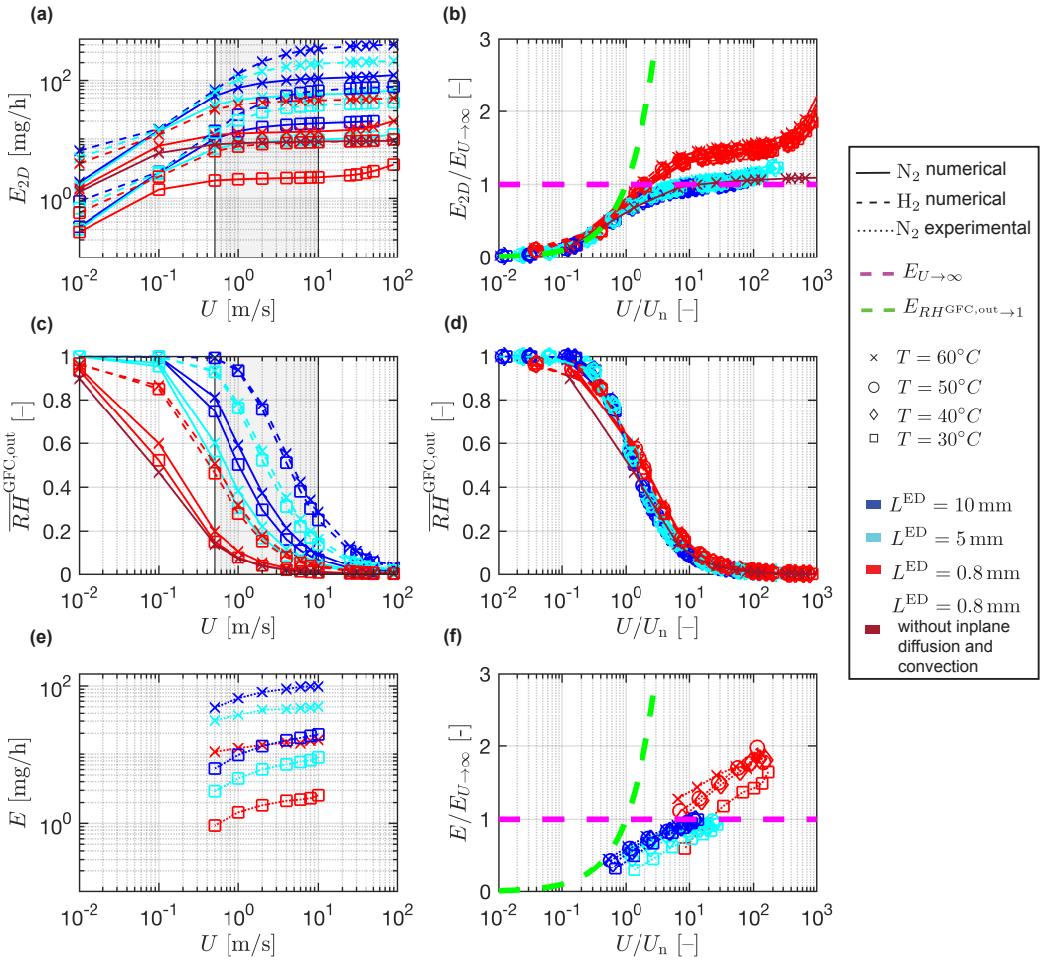


Figure 10: Results of 2D-EvaGDL (2-D model of evaporation in a GDL) as a function of gas speed U: **(a)** evaporation rate, **(b)** normalized results of (a), **(c)** relative humidity at the GFC outlet, **(d)** normalized results of (c). The experimental range of Mularczyk et al. [13] is highlighted with a gray rectangular in (a) and (c). **(e)** Experimental results of Mularczyk et al. [13] and **(f)** normalized results of (e) using parameterizations of simulations in (a-b). For clarity, results are shown only for T=60℃ and T=30℃ in (a), (c) and (e).

$$j^{\mathrm{max}}_{\mathrm{H_2O,t-p}} = M_{\mathrm{H_2O}} \frac{P_{\mathrm{sat}}}{RT} \frac{\mathcal{D}^{\mathrm{GDL}}_{\mathrm{H_2O},X}}{H_{\mathrm{GDL}}}. \tag{16}$$

If this maximum through-plane diffusive flux acts along the entire evaporative domain below the GFC, the maximum total evaporation rate becomes

$$E_{U\to\infty} = M_{\mathrm{H_2O}} \frac{P_{\mathrm{sat}}}{RT} \frac{\mathcal{D}^{\mathrm{GDL}}_{\mathrm{H_2O},X}}{H_{\mathrm{GDL}}} L_{\mathrm{ED}} W_{\mathrm{GFC}}. \tag{17}$$

The second limit in evaporation rate is related to the limit in the capability of the GFC to transport water vapor when the GFC at the outlet is fully saturated with water vapor, that is $RH^{\mathrm{GFC,out}} \to 1$. In

this case, the maximum convective water vapor flux in channel direction can be computed as

$$j_{\mathrm{H_2O},y}^{\max} = M_{\mathrm{H_2O}} \frac{P_{\mathrm{sat}}}{RT} U \tag{18}$$

which, multiplied by the dimension of the GFC, yields the evaporation rate limited by a fully saturated GFC

$$E_{RH^{\mathrm{GFC,out}}\to 1} = M_{\mathrm{H_2O}} \frac{P_{\mathrm{sat}}}{RT} U H_{\mathrm{GFC}} W_{\mathrm{GFC}} \tag{19}$$

Normalized by $E_{U\to\infty}$, we obtain

$$\frac{E_{RH^{\mathrm{GFC,out}}\to 1}}{E_{U\to\infty}} = U \underbrace{\frac{H_{\mathrm{GDL}}}{\mathcal{D}_{\mathrm{H_2O},X}^{\mathrm{GDL}}} \frac{H_{\mathrm{GFC}}}{L_{\mathrm{ED}}}}_{=\frac{1}{U_{\mathrm{n}}}} = \frac{U}{U_{\mathrm{n}}} \tag{20}$$

where $U_{\mathrm{n}} = \frac{\mathcal{D}_{\mathrm{H_2O},X}^{\mathrm{GDL}}}{H_{\mathrm{GDL}}} \frac{L_{\mathrm{ED}}}{H_{\mathrm{GFC}}}$ is the gas speed when $E_{RH^{\mathrm{GFC,out}}\to 1} = E_{U\to\infty}$. In Figure 10b,d, we apply $E_{U\to\infty}$ to normalize the evaporation rate and U_{n} to normalize the inlet gas speed. This normalization tends to lead to an overlap of all curves. This indicates the overall applicability of the derived limits to the evaporation rate. An exception is the smallest evaporation domain that produces a higher evaporation rate than expected from $E_{U\to\infty}$. This can be explained by the additional contribution of the in-plane diffusion close the borders of the evaporative domain, which, relative to the through-plane transport, is the highest for the smallest evaporative domains. We tested this interpretation in a simulation where the advective and diffusive in-plane transport is switched-off inside the GDL (Figure 10a-d, yellow line). The normalized evaporation rate in this simulation overlaps with those of the larger evaporation domains. Furthermore, the second increase in evaporation rates disappears. This is related to the in-plane convective transport that becomes more important inside the GDL with increasing gas speeds. However, this occurs outside the experimental range.

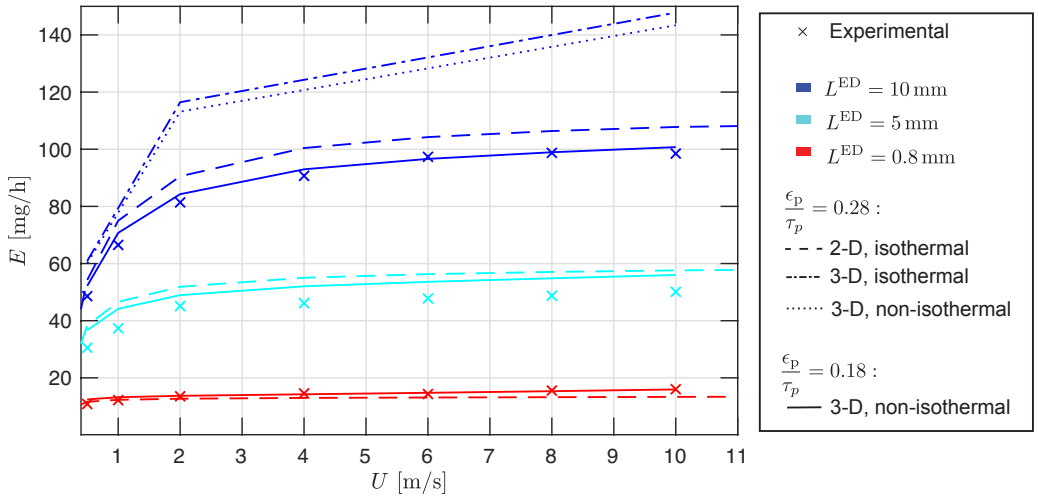


Figure 11: Comparison between experimental results of Mularczyk et al. [13] and results from the isothermal and non-isothermal simulations using 2D-EvaGDL and 3D-EvaGDL with different values of $\frac{\epsilon_{\mathrm{p}}}{\tau_p}$.

Figure 10e-f shows the application of the same normalization to the experimental results of Mularczyk et al. [13]. Generally, the normalization has a similar effect than for the simulation results. This indicates that the 2-D simulation results can explain the experimental to the first order. However, at high gas speeds, the plateau in evaporation rate is not as clear as in the 2-D simulations, especially for the smallest evaporation domain. This motivated us to additionally analyze the role of the part of the evaporation domain below rib and the change in temperature due to latent heat of evaporation using the 3D-EvaGDL model.

We investigated the role of the channel-rib structure for the mass transport in 3-D isothermal simulations. Compared to the 2-D isothermal simulations, significantly higher evaporation rates are generated in the 3-D simulations for the same set of parameters (Figure 11). This is due to the additional water vapor that evaporates along the evaporation domain below the rib (Figure 12c) and transported towards the GFC (Figure 12b-e). This additional contribution to the evaporation rate is the highest at the upper and lower borders of the ED (Figure 12a).

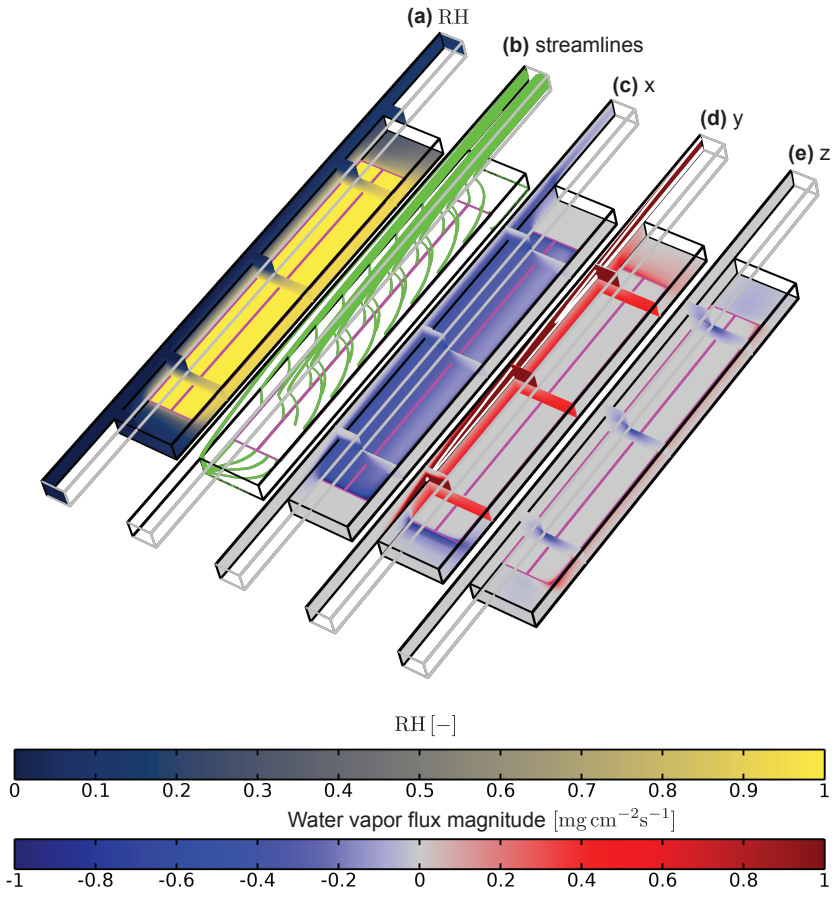


Figure 12: Overview of isothermal simulations results using the model 3D-EvaGDL. **(a)** Relative humidity (RH), **(c-e)** streamlines of total water vapor flux, and **(c-e)** x-,y-, and z-components of total water vapor flux. Gas flow channel (GFC), gas diffusion layer (GDL) and evaporation domain (ED) are indicated.

In 3-D non-isothermal simulations, we investigated the interaction of the heat transport and evaporative water removal. As a consequence of the temperature drop due to latent heat of evaporation, the evaporative rate is reduced compared to the isothermal simulations (Figure 12c). Under nitrogen as a carrier gas, the temperature drop is less than 2 °C (Figure 12a). The minimum temperature is situated directly along the evaporation domain. The maximum difference in evaporation between isothermal and non-isothermal simulation is around 3 percent at L^{ED}, T=60 °C and $U = 10 \mathrm{ms}^{-1}$ (Figure 11). Under hydrogen as a carrier gas, the temperature drop is larger due to the higher diffusivity leading to larger evaporation rates at the same set of operating conditions. Consequently, the difference between isothermal and non-isothermal simulation results become larger. Especially, at operating conditions favoring high evaporation rates, the isothermal simulation overestimate the evaporation rate.

3-D simulations yield higher evaporation rates than in the experiments of Mularczyk et al. [13] (Figure 11). Therefore, the fit between simulation and experimental results appears to be poorer than in Mularczyk et al. [13]. However, we demonstrated that a number of effects have been neglected by the model of Mularczyk et al. [13]. Accounting for conservation of mass and momentum and for variable gas density leads to higher evaporation rates in 2-D simulations. Higher evaporation rates are

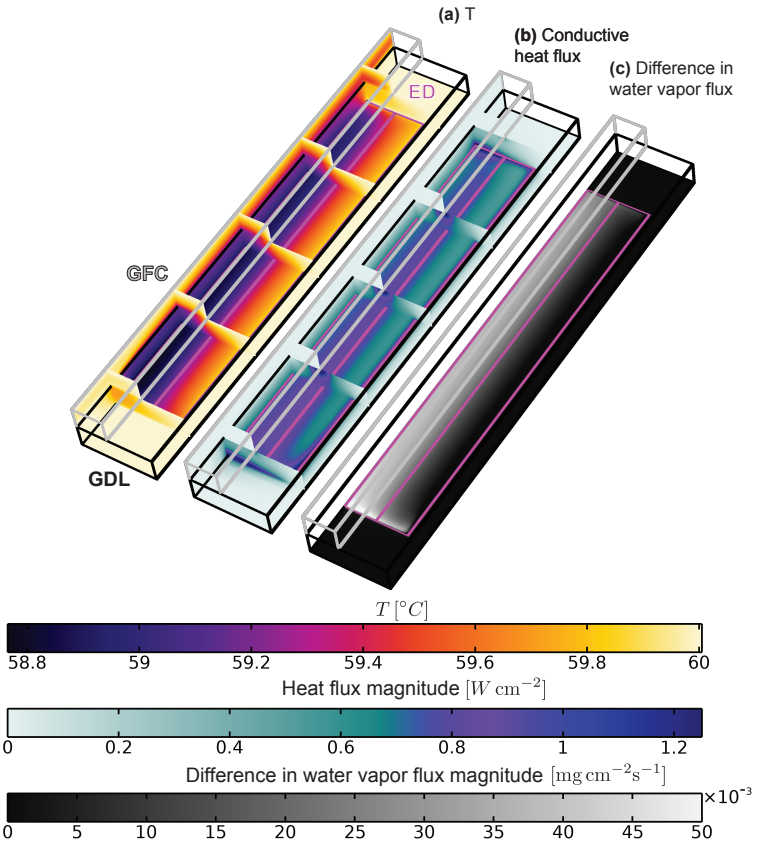


Figure 13: Overview of non-isothermal simulations results using the model 3D-EvaGDL. **(a)** temperature, **(b)** conductive heat flux, and **(c)** difference in water vapor flux between isothermal and non-isothermal solutions. Gas flow channel (GFC), gas diffusion layer (GDL) and evaporation domain (ED) are indicated.



also simulated when the 3-D model is used. Altogether, the model of Mularczyk et al. [13] strongly underestimates the evaporation rate. Finally, accounting for the transport of heat leads to smaller evaporation rates than in the isothermal simulation, although the effect is rather negligible at least for nitrogen as a carrier gas.

The normalization demonstrated that one possible way to reduce the maximum evaporation rate at the highest gas speeds is to use a smaller value for $\mathcal{D}^{\mathrm{GDL}}_{\mathrm{H_2O},X}$, which can be modified by varying $\frac{\epsilon_\mathrm{p}}{\tau_\mathrm{p}}$. The agreement between experimental and non-isothermal 3-D simulation results can be improved through the use of $\frac{\epsilon_\mathrm{p}}{\tau_\mathrm{p}} = 0.18$ instead of 0.28 (Figure 11). These results suggests that the value for $\frac{\epsilon_\mathrm{p}}{\tau_\mathrm{p}}$ used from reference [17] might be too high for the GDL used in the experimental setup of Mularczyk et al. [13]. Pore-scale simulations using GeoDict or similar could reanalyze the porosity and tortuosity, and, hence, the effective gas diffusivity of the GDL.

3.2 Droplet formation and growth

We investigated the formation and growth of a droplet at the boundary between gas flow channel (GFC) and gas diffusion layer (GDL). Due to the production of water in the CL and low liquid water velocity at the GDL/GFC boundary, the capillary pressure and the liquid water saturation increase. This continues until the capillary pressure reaches the maximum (Figure 14a). At this time, the droplet forms. During the subsequent growth of the droplet, the capillary pressure decreases following the Young-Laplace law. This leads to an increase in liquid water velocity (Figure 14c) and fast increase of the droplet volume (Figure 14d). At the same time, the liquid water saturation at the boundary decreases (Figure 14b), following the saturation-capillary pressure relationship (Figure 5).

We conducted the same experiment with different values for the characteristic length scale D_BC in the formulation of the liquid water boundary condition (equation 14).The larger D_c is, the faster is the droplet growth and the sharper is the evolution of P_c, s_liq, u_liq, and V_out at the GFC/GDL boundary (Figure 14).

3.3 GitHub software repository

To make our open-source models of PEMFCs and redox flow batteries available to the research community, we have created a GitHub software repository named ISOMORPH-Electrochemical Cells at `https://github.com/Isomorph-Electrochemical-Cells`. This repository was structured using sub-repositories. One sub-repository was created for the open-source code 1D-MMM [1] called PEMFC-1DMMM `https://github.com/Isomorph-Electrochemical-Cells/PEMFC-1DMMM`. Another sub-repository was created to publish the 0-D code of an organic redox flow battery [18] developed in an European Union project (`https://github.com/Isomorph-Electrochemical-Cells/ORFB-0D-U-I-SoC`).

3.4 Preparation of spin-off company

3.4.1 Re-launch of the website isomorph.ch

The website www.isomorph.ch has been re-launched. The content (text) of the different web pages has been formulated to address different customer groups of our products.

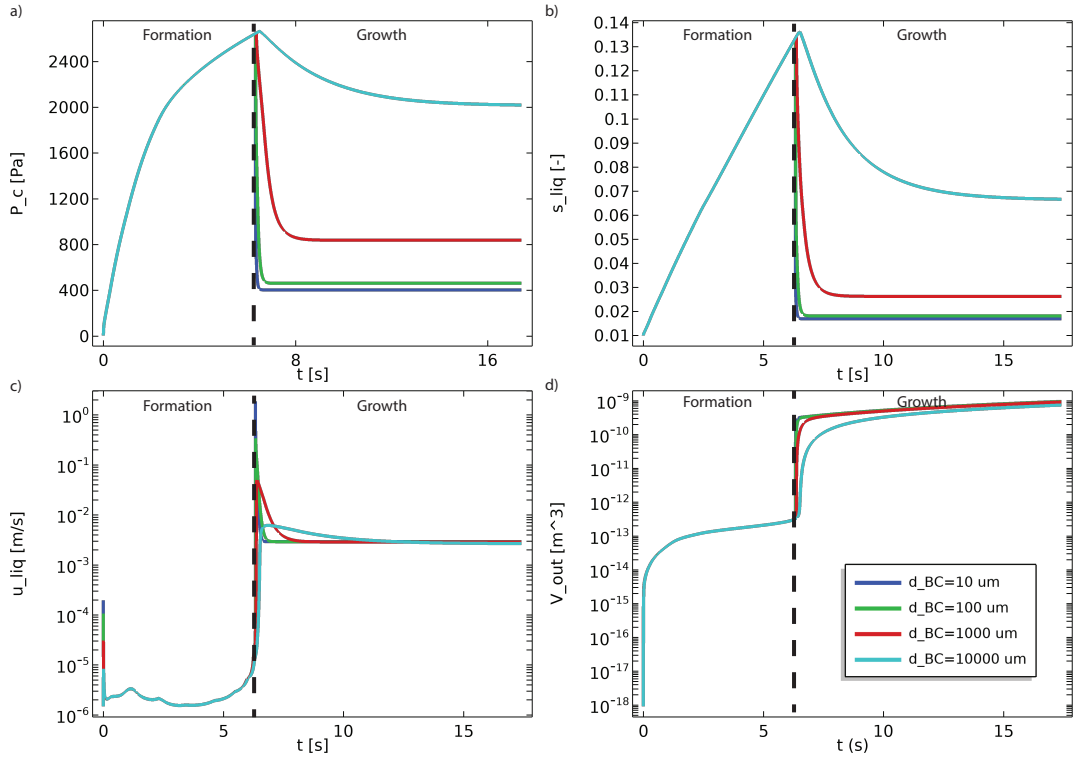


Figure 14: Formation and unlimited growth of a single droplet at the boundary between GDL and GFC: (a) capillary pressure, (b) liquid water saturation, (c) liquid water velocity and (c) water droplet volume.

A new website design has been developed. It is based on to the previous design but the appearance of the page has been improved and the navigation has been facilitated. A screenshot of the new web page is shown in Figure 15.

3.4.2 Development of a marketing strategy

Figure 1 illustrates the value chain of PEMFCs for transport applications. We aim to participate in this value chain by providing computational solutions, particularly by addressing the development of MEAs, the model-based analysis of single test cells, and the simulation of fuel cell stacks.

3.4.3 Development of a business plan

A first version of a business plan of Isomorph has been created that uses the concept of the “Lean Canvas”, describing each product in terms of early adopters, customer segments, customer problem to be solved, alternative solutions, solution, income metrics, unique value proposition, revenue streams, cost structure etc.

(a)



Isomorph - model-based analysis of electrochemical flow cells

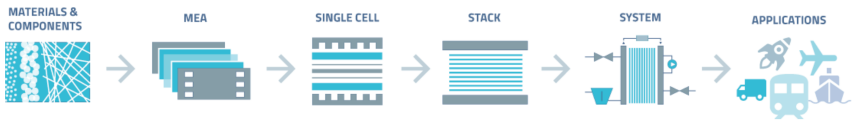
Isomorph is marketing computational solutions to analyze electrochemical flow cells. Our solutions are tailored to the needs of companies and research institutes with a focus on proton exchange membrane fuel cells (PEMFCs) and redox flow batteries (RFBs).

(b)



Proton Exchange Membrane Fuel Cells

Analyze and design proton exchange membrane fuel cells



- **Simulation of coupled transport phenomena**

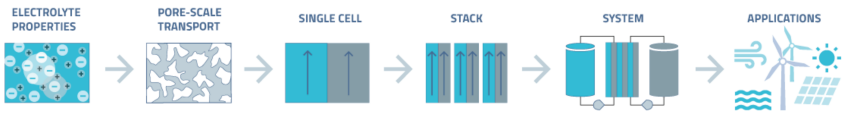
To analyse and design Proton Exchange Membrane Fuel Cells (PEMFCs) the coupled transport phenomena and electrochemical reactions need to be simulated - these are: electrochemical reaction kinetics, charge transport, mass transport, transport and generation of heat, and gaseous and liquid water transport.

(c)



Redox Flow Batteries

Physics-based simulations to optimised RFB



- **Simulation of coupled transport phenomena**

The efficient development and optimization of Redox Flow Batteries requires deep insight into the interplay of various physicochemical processes.

Figure 15: Screenshots of the website : **(a)** home page, **(b)** web page advertising proton exchange membrane fuel cells, **(c)** web page advertising redox flow batteries.

4 Conclusions

The work on the development of different models for evaporative water removal in GDLs and evaporative cooling cell improved our model treatment of gas transport, gas diffusion and evaporation. Another important step was the development of 2-D and 3-D models with incorporation of gas flow channels. These models will be advertised on isomorph.ch.

The conducted work on the liquid water boundary condition needs to be complemented with experimental data to study the formation, growth and detachment of water droplets at the GDL/GFC interface and to find a way to upscale the processes at the pore-level in macro-homogeneous models.

We have succeeded to set up a development version of the website of Isomorph. This improves our web presence and will be used to present products and services on the modelling, simulation and model-based characterization of electrochemical flow cells.

5 Outlook and next steps

5.1 Multi-scale two-phase simulations

To study evaporative removal in GDLs in cases where liquid water enters into the cell, pore-scale simulations are necessary to resolve the air-water interface and the transport of liquid water through the GDL. Additionally, time-dependent models could resolve the the droplet formation and detachment at the GFC/GDL interface. Pore-scale simulations could serve to up-scale the two-phase transport including evaporation to allow for efficient simulations. Such a model could be of great importance to further develop the evaporative cooling concept and water removal in PEMFCs. We are planning to use the Lattice-Boltzmann code PALABOS for such pore-scale simulations (https://palabos.unige.ch/).

5.2 3-D single cell model with electrochemical reactions

The development of a 3-D single cell model during this project focused on the evaporative water removal in a GDL or evaporative cooling cell without electrochemical reactions. In a next step, 3D-EvaCool could be extended to include electrochemical reactions in order to study the change in evaporation rates with increasing current densities and compare the results to the work of Cochet et al. [19].

5.3 Improved model parameterisation and MEA degradation modeling

By presenting our research results we successfully applied for a membership in the European group "Hydrogen Europe Research" (https://hydrogeneuroperesearch.eu), which is the academic working group of the new public private partnership Hydrogen Europe (https://hydrogeneurope.eu). This membership allowed us to participate in the preparation of the European Multi-Annual Work Plan (2021-2027) of Hydrogen Europe Research. ZHAW-ICP was responsible for working out the topic HORIZON-JTI-CLEANH2-2022-03-02 entitled "Innovative and optimised MEA components towards next generation of improved PEMFC stacks for heavy duty vehicles". Next, we successfully participated in the submission of a project proposal led by DLR and the consortium was invited for grant preparation



(EU project ID: 101101433). This new project is entitled "Robust PEMFC MEA derived from model-based understanding of durability limiations for heavy duty applications (PEMTASTIC)". It is planned to start in the beginning of 2023 and it targets the key technical challenges to increase durability of MEAs for heavy duty applications (e.g. fuel cell powered trucks). These challenges are approached with a combination of model-based design and the development of a durable catalyst coated membrane using innovative materials tailored for heavy duty operation at high temperature (105℃).

Our aim is to equip our PEMFC membrane electrode assembly (MEA) models with improved material parameterisations to better reflect properties of commerical MEA components. The goal of our contribution to PEMTASTIC is to model MEA degradation behaviour on the basis of the MEA and single cell performance models developed in this and in previous projects.

5.4 Isomorph.ch

The new website and web services of isomorph.ch will serve for the dissemination and marketing of electrochemical flow cell models. Next steps to make models available to the research community and to companies are:

- Finishing of the product and service descriptions
- Entry of potential customer data into the customer relationship management system
- Setup of a helpdesk software for customer support

5.5 Business plan

The next step is to re-structure the product hierarchy, re-name/re-define the products to better reflect the customer's needs and the combination of model products and services of isomorph.ch.

6 National and international cooperation

During this project, we have established cooperations with the Electrochemistry Laboratory of the Paul Scherrer Institute, in particular with Magali Cochet and Jens Eller. This cooperation enabled us to compare our models with experimental data of evaporation rates in GDLs and evaporative cooling cells. Through this comparison, we were able to improve our models with respect to the transport of gas and water and the treatment of evaporation.

7 Publications

The following peer-reviewed publications resulted from the project:

- Herrendörfer, R.; Cochet, M.; Schumacher, J.O.: Simulation of Mass and Heat Transfer in an Evaporatively Cooled PEM Fuel Cell. Energies 2022, 15(8), 2734. https://doi.org/10.3390/en15082734.



- Mularczyk, A.; Michalski, A.; Striednig, M.; Herrendörfer, R.; Schmidt, T. J.; Büchi, F. N.; Eller, J.: Mass Transport Limitations of Water Evaporation in Polymer Electrolyte Fuel Cell Gas Diffusion Layers. Energies 2021, 14 (10), 2967. https://doi.org/10.3390/en14102967.
- Herrendörfer, R.; Eller, J.; Schumacher, J. O.: 2-D and 3-D Simulation of Water Vapor and Heat Transport Induced by Evaporation in Gas Diffusion Layers of Proton Exchange Membrane Fuel Cells, manuscript in preparation for submission., 2022.

Conference contributions:

- Herrendörfer, R.; Cochet, M.; Boillat, P.; Schumacher, J.O.: 3-D simulation of heat and water transport in PEFCs during evaporative cooling and humidification, European Fuel Cell Forum, 29 July - 2 July 2021. https://digitalcollection.zhaw.ch/handle/11475/22998.
- Herrendörfer, R.; Cochet, M.; Boillat, P.; Schumacher, J.O.: 3-D simulation of heat and water transport in PEFCs during evaporative cooling and humidification, 17th Symposium on Modeling and Experimental Validation of Electrochemical Energy Technologies (ModVal 2021), 20-22 April 2021. https://digitalcollection.zhaw.ch/handle/11475/22417.
- Herrendörfer, R.; Schumacher, J.O.: Advanced characterization of polymer electrolyte fuel cells using a two-phase time-dependent model, 16th symposium on modeling and experimental validation of electrochemical energy technologies (ModVal 2019), Braunschweig, Germany, 12-13 March 2019. https://doi.org/10.21256/zhaw-2790.

References

[1] Roman Vetter and Jürgen O. Schumacher. Free open reference implementation of a two-phase PEM fuel cell model. *Computer Physics Communications*, 234:223–234, 2019.

[2] Roman Vetter and Jürgen O. Schumacher. Experimental parameter uncertainty in proton exchange membrane fuel cell modeling. Part I: Scatter in material parameterization. *Journal of Power Sources*, 438:227018, October 2019.

[3] Roman Vetter and Jürgen O. Schumacher. Experimental parameter uncertainty in proton exchange membrane fuel cell modeling. Part II: Sensitivity analysis and importance ranking. *Journal of Power Sources*, page 126529, May 2019.

[4] M. Cochet, A. Forner-Cuenca, V. Manzi, M. Siegwart, D. Scheuble, and P. Boillat. Novel Concept for Evaporative Cooling of Fuel Cells: An Experimental Study Based on Neutron Imaging. *Fuel Cells*, 18(5):619–626, 2018.

[5] Mike L. Perry, Jeremy P. Meyers, Robert M. Darling, Craig Evans, and Ryan Balliet. Evaporatively-Cooled PEM Fuel-Cell Stack and System. *ECS Trans.*, 3(1):1207–1214, October 2006.

[6] A. Fly and R. H. Thring. Temperature regulation in an evaporatively cooled proton exchange membrane fuel cell stack. *International Journal of Hydrogen Energy*, 40(35):11976–11982, September 2015.

[7] A. Fly and R. H. Thring. A comparison of evaporative and liquid cooling methods for fuel cell vehicles. *International Journal of Hydrogen Energy*, 41(32):14217–14229, August 2016.

[8] Antoni Forner-Cuenca, Johannes Biesdorf, Lorenz Gubler, Per Magnus Kristiansen, Thomas Justus Schmidt, and Pierre Boillat. Engineered Water Highways in Fuel Cells: Radiation Grafting of Gas Diffusion Layers. *Advanced Materials*, 27(41):6317–6322, November 2015.

[9] Antoni Forner-Cuenca, Victoria Manzi-Orezzoli, Johannes Biesdorf, Mario El Kazzi, Daniel Streich, Lorenz Gubler, Thomas J. Schmidt, and Pierre Boillat. Advanced Water Management in PEFCs: Diffusion Layers with Patterned Wettability I. Synthetic Routes, Wettability Tuning and Thermal Stability. *J. Electrochem. Soc.*, 163(8):F788–F801, January 2016.

[10] A. Forner-Cuenca, J. Biesdorf, A. Lamibrac, V. Manzi-Orezzoli, F. N. Büchi, L. Gubler, T. J. Schmidt, and P. Boillat. Advanced Water Management in PEFCs: Diffusion Layers with Patterned Wettability II. Measurement of Capillary Pressure Characteristic with Neutron and Synchrotron Imaging. *J. Electrochem. Soc.*, 163(9):F1038–F1048, January 2016.

[11] Pierre Boillat, Felix Büchi, Lorenz Gubler, Antoni Forner Cuenca, and Celestino Padeste. A method to produce a gas diffusion layer and a fuel cell comprising a gas diffusion layer, March 2016.

[12] Robert Herrendörfer, Magali Cochet, and Jürgen O. Schumacher. Simulation of Mass and Heat Transfer in an Evaporatively Cooled PEM Fuel Cell. *Energies*, 15(8):2734, April 2022.

[13] Adrian Mularczyk, Andreas Michalski, Michael Striednig, Robert Herrendörfer, Thomas J. Schmidt, Felix N. Büchi, and Jens Eller. Mass Transport Limitations of Water Evaporation in Polymer Electrolyte Fuel Cell Gas Diffusion Layers. *Energies*, 14(10):2967, January 2021.

[14] Robert Herrendörfer, Jens Eller, and Jürgen O. Schumacher. 2-D and 3-D simulation of water vapor and heat transport induced by evaporation in gas diffusion layers of proton exchange membrane fuel cells, manuscript in preparation for submission. 2022.

[15] Angelo Esposito, Cesare Pianese, and Yann G. Guezennec. Coupled modeling of water transport and air–droplet interaction in the electrode of a proton exchange membrane fuel cell. *Journal of Power Sources*, 195(13):4149–4159, July 2010.

[16] J. O. Schumacher, Roman Vetter, Luigino Capone, Lorenz Holzer, Adrien Lamibrac, and Felix N. Büchi. Designing multifunctional materials for proton exchange membrane fuel cells. Final Report SI/501129-01, 2017.

[17] Seyed Mohamad Moosavi, Mathias Niffeler, Jeff Gostick, and Sophia Haussener. Transport characteristics of saturated gas diffusion layers treated with hydrophobic coatings. *Chemical Engineering Science*, 176:503–514, February 2018.

[18] Gael Mourouga, Roman P. Schaerer, Xian Yang, Tobias Janoschka, Thomas J. Schmidt, and Juergen O. Schumacher. Physics-based 0D-U-I-SoC Cell Performance Modelfor Aqueous Organic Redox Flow Batteries. *Electrochimica Acta*, page 140185, March 2022.

[19] M. Cochet, A. Forner-Cuenca, V. Manzi-Orezzoli, M. Siegwart, D. Scheuble, and P. Boillat. Enabling High Power Density Fuel Cells by Evaporative Cooling with Advanced Porous Media. *J. Electrochem. Soc.*, 167(8):084518, May 2020.